An Early Clinical Study of Time-Domain Microwave Radar for Breast Health Monitoring

Emily Porter*, *Student Member, IEEE*, Mark Coates, and Milica Popović, *Senior Member, IEEE*

Abstract—**This study reports on monthly scans of healthy patient volunteers with the clinical prototype of a microwave imaging system. The system uses time-domain measurements, and incorporates a multistatic radar approach to imaging. It operates in the 2–4 GHz range and contains 16 wideband sensors embedded in a hemispherical dielectric radome. The system has been previously tested on tissue phantoms in controlled experiments. With this system prototype, we scanned 13 patients (26 breasts) over an eight-month period, collecting a total of 342 breast scans. The goal of the study described in this paper was to investigate how the system measurements are impacted by multiple factors that are unavoidable in monthly monitoring of human subjects. These factors include both biological variability (e.g., tissue variations due to hormonal changes or weight gain) and measurement variability (e.g., inconsistencies in patient positioning, system noise). For each patient breast, we process the results of the monthly scans to assess the variability in both the raw measured signals and in the generated images. The significance of this study is that it quantifies how much variability should be anticipated when conducting microwave breast imaging of a healthy patient over a longer period. This is an important step toward establishing the feasibility of the microwave radar imaging system for frequent monitoring of breast health.**

Index Terms—**Biomedical monitoring, cancer detection, microwave antenna arrays, multistatic radar.**

I. INTRODUCTION

BREAST cancer is the most commonly diagnosed cancer in women, and is responsible for over 40 000 deaths per year in the United States alone [1]. Early detection of breast cancer is vital to successful treatment. The five-year survival rates underscore the importance of early diagnosis: When a breast tumor is diagnosed at a localized stage of growth, the five-year survival rate is 99%; when the cancer is only identified after metastasis, the survival rate decreases to 24% [1]. The standard screening technique for breast cancer is X-ray mammography, but there is significant motivation for developing a complementary modality. X-ray mammography requires the use of ionizing radiation which limits the allowable frequency of scans, involves dis-

comfort and pain due to breast compression, and suffers from relatively poor sensitivity and specificity, especially for women with dense breast tissues [2]. Microwave methods have been suggested as a potential technology that could help to address these shortcomings. Microwave techniques are based on a reported inherent contrast in the dielectric properties (the relative permittivity and conductivity) of healthy and malignant breast tissues over the microwave frequency range [3].

Microwave breast screening and imaging modalities typically fall into one of two categories: tomography or radar. In microwave tomography, the resultant image is a dielectric profile of the tissues within the breast. Microwave radar maps the dielectric scatterers within the breast. Radar methods are less computationally complex, but they do not provide the dielectric properties of the breast that may be of interest. Microwave techniques can be based on measurements in the frequency or in the time domain, with the latter encountered less frequently. Both frequency- and time-domain experimental systems have been reported in the literature, but only a few have been tested on patients [4]–[9]. Notably, in [8], a monostatic radar system was used to obtain microwave images of eight patients, with results compared to their mammograms or magnetic resonance images. Although not all lesions were detected successfully, many were and the microwave images were consistent with known clinical data. Further, microwave imaging was used to monitor the progress of a tumor during chemotherapy in [9]. A tomographic imaging system was used to collect data from more than 500 patient exams, eight of which are studied in [9]. The authors suggest that dielectric property changes are in line with tumor progression and that the overall success of treatment can be predicted after as little as 30 days.

In this study, we test a time-domain microwave radar system for the application of breast health monitoring. We choose time-domain measurements because they may offer advantages over frequency-domain measurements, specifically, faster scan times [10] and more cost-effective measurement devices. Such a microwave monitoring system could be used to scan healthy women on a regular basis. Then, current scans are compared to past scans to identify any irregularities in the breast tissues. The hope is that regular scanning can lead to earlier detection for a higher percentage of the population. Our proposed breast monitoring system is intended for monitoring (healthy) women at high-risk of developing breast cancer, but it could also be used to track the progress of post-treatment therapies.

Our system, initially presented in [11], contains 16 wideband sensors embedded in a hemispherical "cup" in which the breast is placed. In [12] and [13], we presented initial results with data from a small number of patients. Further, in a study presented

*E. Porter is with the Department of Electrical Engineering and Computer Engineering, McGill University, Montreal, QC, H3A 0E9 Canada (e-mail: emily.porter @mail.mcgill.ca).

M. Coates and M. Popović are with McGill University.

in [14], we conducted breast scans of one patient daily over the span of one month, and compared them to scans taken in the same manner with a heterogeneous breast tissue phantom of known and stable dielectric properties. Each day, the phantom was repositioned in the radome, to mimic the patient's daily breast repositioning. Despite the repositioning, the phantom data were highly consistent over all measurement days. In contrast, the patient data exhibited significant variability, suggesting that patient-related changes, possibly due to tissue variations, were detected. Finally, in prior work we also demonstrated successful imaging of tumors when the phantom, which included a skin layer, was repositioned in the ultrasound immersion within the radome between each scan, as would occur in a patient-monitoring scenario [15].

In this study, we report on microwave monitoring of healthy patients using the time-domain radar system. We present and examine an expanded clinical dataset obtained as follows. We performed multiple breast scans on 13 women (26 breasts) over an eight-month period. Thus, we have emulated a monitoring scenario in which the women undergo regular breast scans. To our knowledge, no similar dataset was previously reported for a microwave breast imaging system applied to healthy patients. This study has several added challenges when compared to the one presented in [14], mainly attributed to working with multiple patients instead of one. For example, different volumes of immersion medium were required for each patient, and since the conducted study spanned a longer period of time, it was necessary to replace the immersion medium gel between patient visits.

The primary goal of this study was to determine how much variability should be anticipated when conducting microwave breast imaging of a healthy patient over a longer period. We explore how the system perceives the changes that occur due to the monthly intervals. These changes are due to a combination of factors including both biological variability (e.g., tissue variations due to hormonal changes or weight gain) and measurement variability (e.g., inconsistencies in breast positioning, system noise). Although we strive to minimize the measurement variability, we do not attempt to isolate the biological factors. For each patient breast, we process the results of the monthly scans to quantify the variability in both the raw measured signals and in generated images. We analyze variability by calculating the Pearson correlation between time-domain signals, the structural similarity index between breast images, and the maximum pixel intensity in the images.

In the following sections, we introduce the measurement system, describe the clinical trials and participants, and then provide an analysis of the resulting scan data. We compare the collected signals and reconstructed images for successive scans of the same breast over time. The main conclusion of the study is a summary of the anticipated variability in time-domain microwave measurements, conducted over a period of multiple months, of the same breast. As a secondary outcome, the study allowed us to fine-tune the system and identify procedures and parameters to optimize the design of the next-generation prototype.
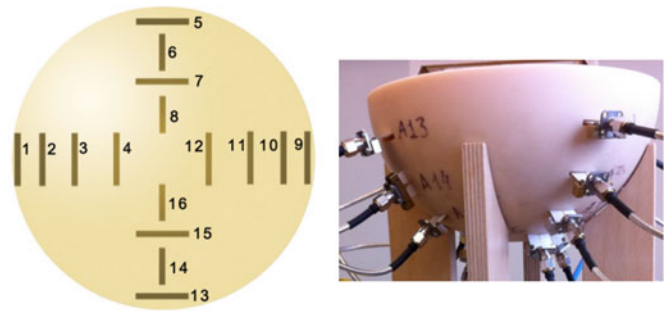

Fig. 1. Schematic drawing of the radome (left), with cross-polarized and copolarized antenna positions labeled numerically. A1, A5, A9 and A13 are closest to the height of the chest wall; and photograph of the radome and antenna array (right) in a wooden holder.

II. System and Trial Description

In this section, we describe the monitoring prototype, the patient volunteers, and the measurement protocol for collecting the breast scans.

A. Time-Domain Microwave Radar System

The system, initially presented in [11], operates as in typical multistatic radar. A short-duration (70 ps length full-width at half-maximum) pulse is generated in the time-domain. The pulse is reshaped using a passive microstrip line [16] in order to focus its frequency spectrum over the 2–4 GHz range. This selected spectral range constitutes a compromise between losses of in-tissue propagation (prohibitively large at higher frequencies) and the insufficient spatial resolution at low frequencies. After reshaping, the pulse is amplified before being fed into a transmitting antenna. The wave propagates through the breast tissue and is received by another antenna and recorded by an equivalent-time sampling oscilloscope. An automated 16×2 electromechanical switching matrix selects each antenna in turn to transmit, while the remaining antennas act as receivers.

In our system, the sensors are resistively loaded traveling-wave antennas, designed specifically for biosensing applications [17]. The antennas are embedded in a hemispherical dielectric radome, which fixes their location securely in place. The breast is positioned in the bowl of the radome. The array is composed of 16 antennas, arranged with four in each quadrant of the radome, as illustrated in Fig. 1. Antennas are positioned in cross-polarized and copolarized orientations in order to maximize reception of the scattered wave.

B. Patient Volunteers

We recruited 13 volunteers to participate in the trial; the study was approved by the Research Ethics and Compliance Office at McGill University. The inclusion criteria for involvement in the study were as follows: legal age, no personal history of breast cancer or breast surgeries, no breast implants, no pacemaker, no nonremovable piercings in the area. All of the volunteers were healthy for the duration of the clinical trial. Our present trials include only healthy patients so that we can evaluate our system's response to healthy tissues. Only after this response has

TABLE I
PATIENT INFORMATION: AGE, BRA CUP SIZE, NUMBER OF VISITS, AND
DURATION OF PARTICIPATION IN THE CLINICAL TRIAL

Patient #	Age	Cup Size	# Visits	# Months
1	21	C	4	6
2	25	D	4	6
3	24	C	5	7
4	44	C	6	8
5	54	B	4	8
6	55	B	2	2
7	23	B	6	6
8	44	C	6	5
9	38	B	4	5
10	26	A	5	6
11	22	B	4	6
12	27	C	3	3
13	76	B	4	4

Fig. 2. Patient interface table with measurement system underneath (left) and a patient getting her breast scanned with the system (right) [12].

been well examined can we properly investigate the system's response to developed malignant lesions; this will constitute a study organized and approved for a separate group and type of volunteers. The 13 patient volunteers were aged 21 to 76, with bra cup sizes from A to D. Patient visits were scheduled to occur on a monthly basis to coordinate with the menstrual cycle. Due to limitations in their availability, not every person was scanned every month. A summary of the patient and visit information is provided in Table I.

C. Measurement Procedure

All breast scans were recorded with the same measurement parameters: each signal contained 1024 samples and was sampled at 40 GSa/s (sampling period $T_s = 25$ ps), with a pulse repetition rate of 1 MHz. Each breast scan is composed of 240 signals, collected from the 16×16 multistatic antenna array. Photographs of our system prototype and of a volunteer getting her breast scanned are shown in Fig. 2.

We also note that all right breast scans were recorded with 16 averages per signal and all left breast scans were recorded with 32 averages. Using 32 averages lowers the measurement noise in the recorded signal as compared to using 16 averages; however, the measurement time is longer. Thus, although not a component of the current study, this data collection scheme enabled examination of the tradeoff between the time and noise parameters. In our previous work [18], successful imaging was achieved regardless of the number of averages.

For all scans, ultrasound gel was used as the immersion medium. Its purpose is to fill any air gaps between the irreg-

ularly shaped breast and the radome. The measured dielectric properties of the gel at the centre frequency 3 GHz are: relative permittivity $\varepsilon_r = 68$, conductivity $\sigma = 3$ S/m, and loss tangent $\tan\delta = 0.26$. Due to its loss factor, the gel attenuates multiple reflections between the two interfaces. The same volume of ultrasound gel was used for all scans (left breast and right breast) conducted during each patient visit. We measured the gel volume during the first visit, and used approximately the same amount for subsequent visits, but there were small variations in volume and distribution. The amount of gel required is determined by the breast size, thus the volume of gel used was patient-specific.

At each visit, each breast was scanned three times: twice successively with no change in parameters, and a third time after the patient moved and repositioned their breast in the radome. There were a total of 57 patient visits, resulting in 82 080 individual signals. The two consecutive scans of each set of scans are denoted as baseline (BL1, BL2) scans. These scans differ only in terms of measurement noise. The third scan, taken after repositioning (AR), has the added variation due to the breast position relative to the ultrasound gel and radome. For the patient repositioning, the patient was asked to remove their breast and then reposition it into the radome, mimicking the effect of positioning the breast on a new scan date. The results on system robustness to movement and other measurement uncertainties, e.g., horizontal and vertical noise, were presented in [19]. Thus, for each patient visit, unless otherwise noted, we only consider the baseline (BL1) scans from here on.

Due to a failure of measurement equipment, specifically, the oscilloscope, partway through the clinical trial study, we had to change the setup configuration such that the data was recorded on a different scope channel. In experiments with more advanced systems, a similar malfunction might occur or it may prove necessary to use multiple measurement systems, so it is useful to understand the anticipated impact on measurement variability. In particular, we began the trials using Channel 1 (Ch1) to record the data. Out of the 57 patient visits, 38 were recorded using Ch1. Late in the trials we had to switch to recording the data on Channel 2 (Ch2). Data for the remaining 19 patient visits was recorded on Ch2. All recording parameters were maintained consistent regardless of which channel was used. After analyzing the data, we found that in images generating using differential baseline signals, the mean maximum pixel intensity of all images was -32.6 dB for Ch1, and -31.5 dB for Ch2. Although the Ch2 dataset is smaller, this does appear as a source of noise in the data. However, as will be shown, imaging results with scans of the same patient on different days (SZ) compared to scans of the same volunteer taken on the same day (BL) vary by more than -32 dB. Thus, changes due to the channel of recording are not thought to be a contributing factor to the similarity (or dissimilarity) between scans of a given patient.

D. Notation

For clarity in the recorded data, we introduce the notation for the various trial parameters. Volunteers are denoted VY, with $Y = 1 : 13$. Within the scans from each patient volunteer, the subsequent scans are denoted SZ, $Z = 1 : i$, where i is equal to
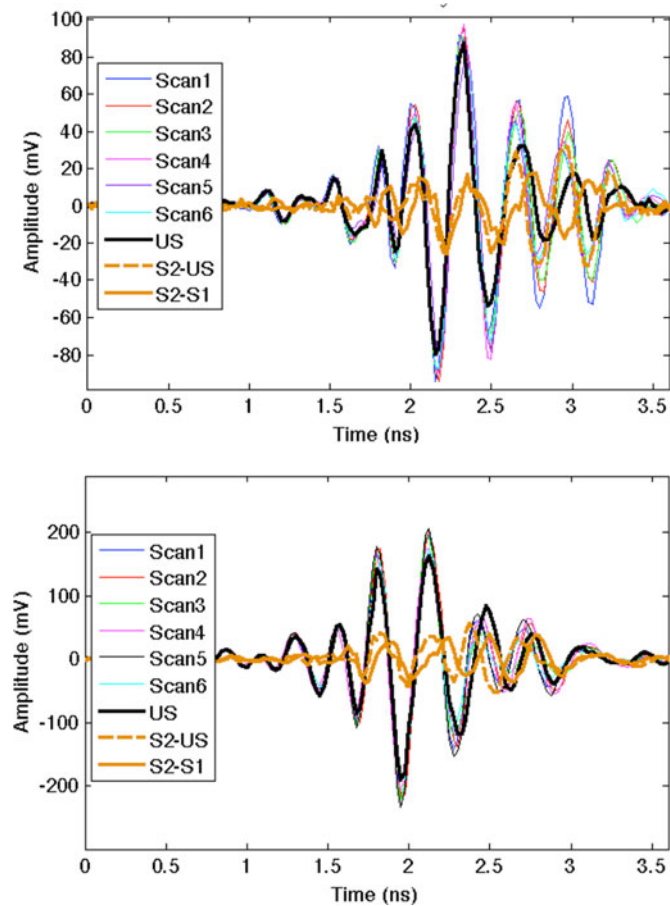
Fig. 3. Sample plots of aligned collected signals for each of the six visits (S1:S6) of V7, left breast: A_1A_4 (top) and $A_{13}A_{15}$ (bottom). The corresponding signal from the same antenna pairs from a scan of the radome filled with ultrasound gel (US) is also shown for comparison (bold, black line). The difference signals between scans of the volunteer (S2-S1) and between a volunteer scan and the ultrasound-filled radome (S2-US) are also shown (bold, orange line).

the number of visits for that volunteer (e.g., if the patient visited on six occasions, as did V4 in Table I, then $i = 6$).

Further, we name the antennas in the radome as shown in Fig. 2. In order to properly interpret the recorded signals, we must know where the antennas are located relative to each other. A transmit-receive antenna pair is denoted as $A_T A_R$, where T = antenna transmitter number and R = receiver number. For example, $A_3 A_4$ is the transmit-receive antenna pair for when antenna number 3 is the transmitter and number 4 the receiver.

III. SIGNAL ANALYSIS

We first examine the recorded signals from each scan, and then analyze the images reconstructed from this data. Throughout this study, particular attention is paid to V4, V7, and V8. These volunteers were scanned monthly, having six scans each and resulting in more signal data than for other volunteers.

We begin by visual inspection of the collected signals. In Fig. 3, we plot sample received signals for two select antenna pairs for volunteer V7, visits S1 to S6, and for a scan of the radome filled with ultrasound gel for reference. The signals

shown here have undergone alignment. The time axis shows the signal from when the oscilloscope starts to record. The length of the signal shown is sufficient to cover both the early- and late-time responses. The pulses shown have contributions from various signal components, including scattering from the radome, ultrasound, skin, breast interior, and waves traveling directly between antenna pairs. The early time portion of the pulses are most significantly due to the direct path traveled from antenna to antenna when the antennas are next to each other and a surface wave traveling along the radome or ultrasound gel between antennas; further, if there is a breast present, there is a contribution from the ultrasound-skin reflection. The later time signals (when the pulse envelope is decreasing) are due to the transmission/reflection of the breast tissues, and possible noise sources.

As expected, the antenna pair with transmitter and receiver further apart (A_1A_4) results in collected signals with lower amplitude and time delay relative to antenna pairs that are closer to each other ($A_{13}A_{15}$). We also note that wave polarization affects the shape and amplitude of the transmitted signals: As the radome is hemispherical, and antennas point toward the center of the sphere, the angle between A_1 and A_4 is greater than that between A_{13} and A_{15}. In other words, the angular orientation of antennas relative to one another varies for different pairs.

From the plots in Fig. 3, we see that the signal trends are similar for each visit. Some variation in the collected signals on different visit occasions is expected due to different volume and distribution of ultrasound gel, slight changes in patient positioning within the radome, and possible changes in tissue properties.

In Fig. 3, the signals recorded with the radome filled with ultrasound gel (without a breast present) have similar early-time response to the volunteer scans, while the later-time response does vary. In order to explore the removal of the direct pulse, surface wave, and skin reflection, Fig. 3 also plots two difference signals. The difference between the signal from the given antenna pair for two volunteer scans (S2 and S1) is shown, along with the difference between S2 and the ultrasound gel scan (US). In both cases, the early-time signal is significantly reduced. The two difference signals are also closely matched in amplitude. Similar results are found for the other antenna pairs. The monitoring application by its design involves system calibration using patient scans. However, at the onset of the screening history, in the absence of earlier scans, calibration with ultrasound gel scans can remove the majority of unwanted signal content.

A. Comparison of Signals From Different Scans

We now quantify the similarity between signals collected from scans on the same breast over multiple patient visits.

First, we calculate the cross correlation between signals. For each scan, there are 240 signals recorded, one for each transmit-receive antenna pair. When comparing two scans, we compare on a corresponding signal-to-signal basis, i.e., compare A_1A_2 from scan 1 (S1) with A_1A_2 from scan 2 (S2), then A_1A_3 from S1 with A_1A_3 from S2, etc. The cross correlation is normalized
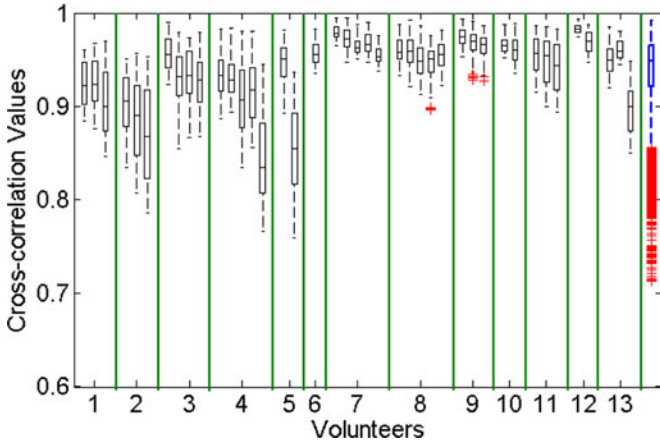
Fig. 4. Boxplots for each SZ of each volunteer (VY) showing the median (centre horizontal line of each box), and $\pm$ 2.7 standard deviations (whiskers) of the maximum cross correlation of SZ with S1 for the 50 antenna pairs in S1 with the largest peak amplitude. Vertical green lines demarcate the volunteers. Also shown, in blue, is a boxplot of maximum cross correlation values comparing signals intervolunteers. Note that red crosses indicate outliers.

to the value of the autocorrelations at zero lag. We obtain the cross correlation (at best time alignment) for the signals from each antenna pair

$$c_{TR}^{SZ} = \max_{t} \frac{\langle (A_T A_R)^{SZ}, (A_T A_R)_t^{S1} \rangle}{\left|(A_T A_R)^{SZ}\right| \left|(A_T A_R)^{S1}\right|} \quad (1)$$

for $T = 1:16$, $R = 1:16$, $T \neq R$

where c_{TR}^{SZ} is the computed cross correlation value between $(A_T A_R)^{SZ}$, the signal from antenna pairs $A_T A_R$ in scan SZ, and $(A_T A_R)^{S1}$, the signal from antenna pairs $A_T A_R$ in scan S1, $\langle \cdot \rangle$ denotes the inner product, and $|\cdot|$ is the ℓ^2-norm. The value c_{TR}^{SZ} is obtained is at the single time shift, t, that maximizes the inner product. This procedure results in 240 cross correlation values for each scan SZ with the first scan S1 as the reference (one value per antenna pair). We focus our analysis on the 50 antenna pairs that have the largest peak amplitude; more specifically, those pairs $A_T A_R$ that have the largest signal value over all points in time.

We do not examine mean or minimum cross correlation values because signals that are close to the noise floor of the system or the background clutter level may vary significantly between scans. These are low amplitude signals that do not contribute to image generation and analysis sufficiently to impact the results. The aforementioned procedure is done to calculate the cross correlation between S1 and SZ ($Z = 2:i$, where i is the number of monthly scans for a given patient) from multiple patient visits for each volunteer. The resulting ranges of maximum cross correlation values are plotted in Fig. 4.

From Fig. 4, the highest maximum cross correlation value between scans of the same patient is 0.9947, and the lowest is 0.9241. It is also noticeable that some scans are more similar to S1 than others, and that this effect is not dependent on the time elapsed between scans. Some volunteers have significantly higher maximum cross correlation values than others. For instance, for V2 all values are below 0.96 while for V9 all are

above 0.98. The first five volunteers (V1 to V5) all had their initial breast scan during the first week of clinical trials, when the placing of the breast in the immersion medium was still being optimized. This could have led to differences between the first scan S1 and later scans SZ for V1 to V5.

Also plotted in Fig. 4, is the set of maximum cross correlation values obtained when comparing scans intervolunteer (shown in blue). This indicates that most signals (i.e., from specific antenna pairs) are similar across all scans of a given volunteer.

In terms of breast health, the maximum cross correlation of recorded signals may not be a particularly useful metric, because the presence of a tumor is not anticipated to significantly alter the signal shape or amplitude. However, we should have in mind that the cross correlation provides an indication of the repeatability of the measurement procedure.

We also calculate the cross correlation values for two further scenarios: 1) the difference signal of (SZ – S1) with SZ, and 2) the difference signal of (SZ – US) with SZ, for all scans of all volunteers. The difference (SZ – S1), for SZ and S1 from the same volunteer, results in a residual signal that has effectively eliminated the components of the signals that appear in both SZ and S1 scans, namely, the direct pulse, the surface wave, and, the skin reflection. On the other hand, the difference of SZ and US results in a residual signal that has removed the direct pulse and the surface wave. We note that the difference signals are only meaningful if the two scans are first time-aligned, as they are here.

For the top 50 antenna pairs, as is presented in Fig. 3, the median values for the cross correlation of (SZ – S1) with SZ, for each visit, range from $[-0.29, 0.45]$, with a median over all scans of all volunteers of 0.05. As the signals from the S1 and SZ are known to be similar (see Fig. 3), these low cross correlation values suggest that calibration with S1 effectively eliminates undesirable components of the SZ signal (skin reflection, direct pulse, surface wave) that are also present in the S1 scan. Similarly, the median values for the cross correlation of (SZ – US) with SZ fall within $[-0.19, 0.52]$, with a median of 0.23. This demonstrates that dominant components of the signal (the direct pulse and surface wave) have been removed with US calibration; however, the removal is not as successful as with the S1 calibration (due to the lack of removing the skin reflection).

B. Relative Permittivity Estimates

We use the radome filled with ultrasound gel (with no breast) as a calibration to calculate the propagation delay for various antenna pairs with a propagation medium of known material properties. We can then estimate the average relative permittivity, ε_r, of a breast when it is placed inside the radome. The calculation is performed at the center frequency of our application, 3 GHz, and neglects dispersion. More specifically, for a single transmit-receive antenna pair wherein the antennas are located on opposite sides of the breast, we can write

$$\frac{d_r}{v_r} + \frac{d_{us1}}{v_{us}} + \frac{d_b}{v_b} = t_1 + \tau_1 \quad (2)$$

TABLE II
AVERAGE BREAST ε_r FOR EACH OF THE FIRST FOUR MONTHLY VISITS
(S1:S4): LEFT BREAST FOR V7 AND V8

Volunteer #	Scan S1	Scan S2	Scan S3	Scan S4
V7	27.2	27.0	27.2	26.4
V8	25.6	24.7	28.6	26.2

Values accurate to within $\pm$ 1.4.

TABLE III
AVERAGE BREAST ε_r FOR THE 26 BREASTS FROM ALL VOLUNTEERS,
SEPARATED BY AGE GROUP

Age Range	Average ε_r
< 30	31.7
30–49	29.3
50+	28.2

Values accurate to within $\pm$ 1.4.

TABLE IV
AVERAGE BREAST ε_r FOR ALL VOLUNTEERS, BY CUP SIZE

Cup Size	Average ε_r
A–B	28.7
C–D	32.2

Values accurate to within $\pm$ 1.4.

where d_r, d_{us1}, and d_b are the total wave propagation distances through the radome material, the ultrasound gel and the breast, respectively, for the given transmit-receive antenna pair positions. Similarly, v_r, v_{us}, and v_b are the average propagation speeds in the three media. The time of propagation of the wave is t_1, and the jitter in the recorded signal is τ_1. This equation can be compared to the one written for the calibration case, when the radome is filled with ultrasound gel only

$$\frac{d_r}{v_r} + \frac{d_{us2}}{v_{us}} = t_2 + \tau_2 \qquad (3)$$

where d_{us2} is the distance traveled through ultrasound gel and t_2 is the signal arrival time in this scenario. τ_2 is the jitter in the recorded data. In these equations, d_r is a fixed constant, as is v_r (the radome size and dielectric properties are well known). Similarly, d_{us2} and v_{us} are precisely known. The breast size, d_b can be physically estimated, and d_{us1} solved for since the radome size is known. Subtracting (2) from (3) and neglecting jitter, we can solve for v_b in terms of d_b and a difference in time. From this velocity, the average relative permittivity can be calculated. The average relative permittivity can be calculated for several transmit-receive antenna pairs of any given breast scan, and then averaged to reduce the contribution of the random jitter. Here, four antenna pairs are used to obtain a final value.

The estimate ε_r is dependent on accurate information of the signal arrival time. As the system operates in the time-domain, there is an inherent level of jitter in the collected signals that cannot be completely compensated for. The estimate is further affected by the imprecise knowledge of the breast volume and shape, and, consequently, by the thickness and the distribution of the surrounding ultrasound gel layer. Therefore, the exact propagation time within these two media is not precisely known. In the worst-case scenario, i.e., with no jitter compensation and the maximum uncertainty in ultrasound gel thickness (1 cm), we calculate that the error in estimated ε_r is approximately ± 1.4.

In Table II, we provide an example for V7 and V8 that shows how the estimated average relative permittivity changes over four consecutive scans of the same breast. These values are calculated from the average value over the three scans of a given breast from each patient visit (BL1, BL2, and AR). Table II shows that the ε_r values experience minor monthly variations; in fact, this level of change is insignificant relative to the error in the calculation.

Next, we compute the average ε_r for all breasts within given patient age categories. The results are presented in Table III. Despite the small sample size, we do see that the average ε_r decreases with increasing age as is expected (the younger women

are more likely to have denser breast tissues) [20]. Finally, the average relative permittivity is presented based on breast size in Table IV. This table suggests that, for our limited patient population, the women with smaller breast sizes have, on average, slightly less dense breasts than those with larger size. These preliminary observations will be tested on a larger sample size in future studies.

IV. IMAGE GENERATION AND ANALYSIS

A. Image Reconstruction

The signals are preprocessed before their use in an imaging algorithm. First, the signals are cropped to begin just before the start of the main pulse; only the region of interest is retained. The signals are then filtered with a low-pass filter at 4 GHz. Finally, the signals are time-aligned to remove jitter. This is achieved by aligning signals based on a simultaneously recorded clock signal, and by using cross correlation techniques. A detailed description of the time-alignment method can be found in our previous work [18].

Images are generated using a differential radar method as follows. In order to generate images using this method, we need to have two scans obtained with our system: one as a "calibration" dataset, and one as the signal set. All signals from the calibration and signal sets are time-aligned with respect to each other, as in

$$\tilde{X}_j^{SZ}(t) = X_j^{SZ}(t + \tau) \qquad (4)$$

where τ is the time shift (with units of samples) that provides the maximum cross correlation of X_j^{SZ} and X_j^{S1}: X_j^{S1} is the set of signals from scan S1, X_j^{SZ} is the set of signals from scan SZ, $\tilde{X}_j^{SZ}$ is the time-aligned X_j^{SZ}, $j = 1 : 240$ is the signal index which is the same for all scans, and $Z = 2 : i$. This compensates for any time offsets that occur between scan times. The time-aligned signals are then subtracted, resulting in a differential signal that has been removed of any systematic sources of noise

or clutter. For a given scan SZ, the differential signal set δ^{SZ} is calculated as follows, using S1 as the calibration scan

$$\delta_j^{SZ} = \tilde{X}_j^{SZ} - X_j^{S1}. \tag{5}$$

This resulting differential signal is then input into the imaging algorithm.

In this study, we use the delay-multiply-and-sum (DMAS) algorithm [21] to reconstruct images of the breast. The voxel resolution is set to 2 mm^3, and the imaging area is the same size as the radome. We generate images using the first patient visit for each patient (S1) as the calibration scan for later patient visits of that same patient (SZ, $Z = 2 : i$). The imaging parameters used to calculate time delays in the algorithm are based on the relative permittivity estimates for each individual patient, and include the layer of ultrasound gel. Full 3-D visualizations are produced from a sequence of 2-D cross-sectional images.

B. Imaging Results

We next present sample images, generated using the differential signals input into the DMAS algorithm. All images are shown as 2-D coronal slices, with red regions representing areas of high scattering and blue regions indicating weak or no scattering. More specifically, as we obtained the images using a differential signal, they demonstrate the differences between the two breast scans from which they are generated. In this way, scattering regions in the images do not necessarily indicate scatterers within the breast, but they do indicate differences in the tissue in that region between the occasions of the two breast scans. For example, if there were no measurement uncertainties or noise and no breast tissue changes in between scans, the differential signal would identically equal zero, and the reconstructed image, when using the same scale, would be entirely dark blue.

In Fig. 5, we plot a sample slice of the differential images generated for the left breast of volunteer 9 (V9), in both linear and log scale. The slice is taken at a depth of 21 mm from the chest wall toward the nipple. The imaging region is delimited by the radome walls; the radome boundary may coincide with the location of the skin, depending on breast size. V9 participated in the clinical trial for a total of four scans on different occasions. Thus, the three differential images were generated using scan 1 as calibration, and scans 2, 3, and 4 as the datasets. These three images are normalized to the peak pixel intensity of an image formed by processing scan 1, calibrated with a scan of the radome completely filled with the immersion medium. Although it may include greater clutter due to the effects of reflections from the skin-gel interface, such an image provides an indication of the maximum scattering induced by the presence of a breast, and thus its maximum pixel intensity serves as a reasonable normalization value. Since all images in Fig. 5 are normalized to a common value, the effect is merely a change in the scale. The image contents include changes due to tissues, along with system-related noise sources (for instance, breast position and random measurement noise).

As is seen from Fig. 5, the differential images shown in linear scale suggest that the scans S2, S3, and S4, are all similar to
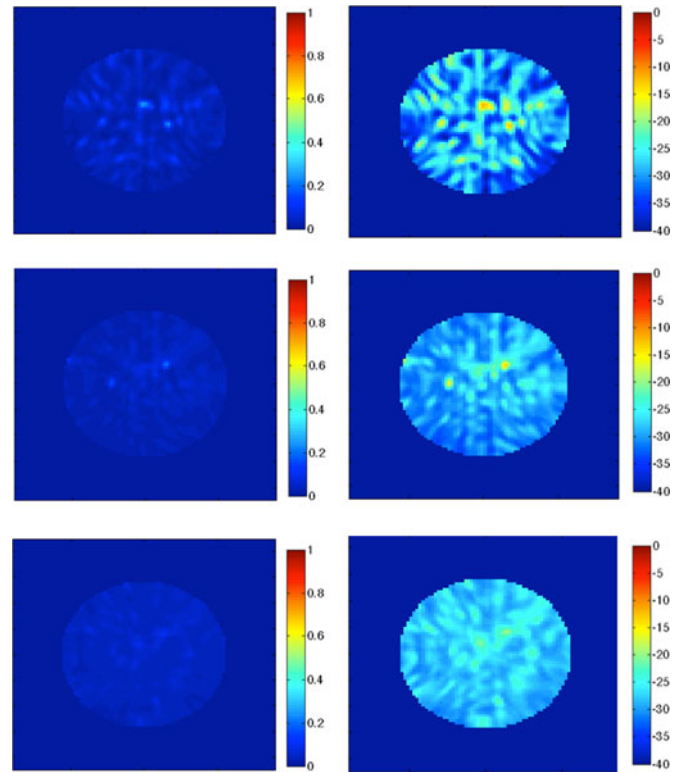

Fig. 5. Reconstructed images for V9, left breast, for scan 2 (top), scan 3 (middle) and scan 4 (bottom): in linear scale (left column) and log scale (dB, right column). The images are generated using scan 1 as calibration.

S1. We also note that there are small visible changes in the images, for instance, in the image for S2 there are two brighter regions just above and to the right of the center of the image. However, in the slices of S3 and S4, these brighter areas are no longer noticeable. In the context of monitoring a patient, healthy tissue changes may appear in the images over time; these should, however, vanish in the long term, unlike the possibly developing malignant growth.

The image slices plotted in log scale, in Fig. 5, allow us to better quantify the results. For S2, the maximum pixel intensity found in the differential image is at −12 dB relative to the maximum pixel intensity for S1 calibrated with a breastless system. Similarly, the maximum pixel intensity for S3 is −14 dB and for S4 is −16 dB. We note that the results do not necessarily degrade as the scan occasions become further apart in time. More importantly, it is evident that this maximum pixel intensity value itself is not useful for identifying the presence of malignancies without further information. A near-future study is planned to characterize the relationship between pixel intensity in a differential image and tissue changes in the breast, i.e., what pixel intensity values can result from healthy tissue changes, and what values are more likely to indicate a malignant growth.

C. Maximum Pixel Intensity

Continuing the analysis of the maximum pixel intensities of the differential images, we next provide a comparison of the maximum intensities for each volunteer over each scan. At this
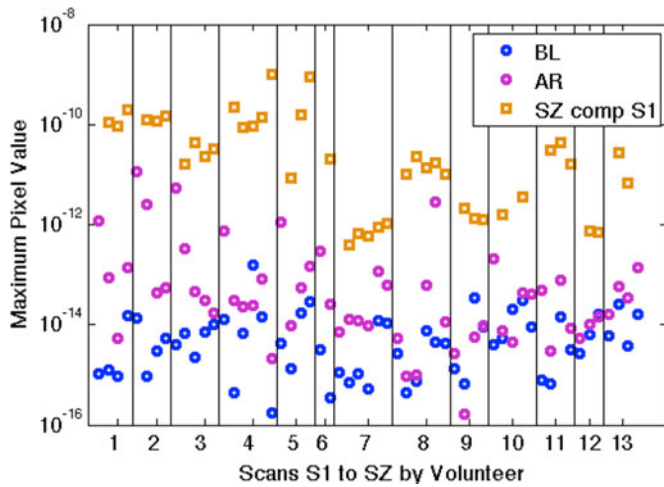
Fig. 6. Maximum pixel intensity values for two scans taken on the same day without patient movement (baseline; BL; blue circles), two scans taken on the same day before and after patient repositioning (after repositioning; AR; magenta circles) and two scan taken on different days (SZ calibrated with S1; denoted as "SZ comp S1;" orange squares), for all scans of all volunteers. The vertical black lines separate the data by volunteer: the first four blue points (and three orange points) are for V1, and so on up to V13.

stage, we take advantage of the multiple breast scans that were collected during each patient visit. As stated in Section II-C, during each visit, three breast scans were taken of each breast. The first two were taken consecutively, and the third after the patient repositioned her breast in the radome. Generating images that use the first two of these breast scans, one as the dataset and the other as the calibration set allows us to identify the maximum pixel value that is present in the images when the two scans are as similar as possible (no patient movement, no changes in tissue, no changes in immersion medium volume or distribution, and no changes in measurement procedure). Thus, this represents the "Baseline" (BL) scenario, in which the only information present in the images is noise, and it provides us with the minimum level of change that can occur between two scans recorded with our system. Similarly, the after-repositioning scenario (AR) allows identification of the differences in the images due to the breast position. AR images are generated using the after-repositioning scan data calibrated with the first scan taken on that day (prior to repositioning).

In Fig. 6, we present the maximum pixel intensity values for image slices of the left breast for all volunteers. There are three parts to the data for each VY: 1) The baseline scenario (as described above) wherein the maximum pixel intensity is representative of the case in which there are no breast tissue changes between scans and no change in breast position; 2) The after repositioning scenario in which the scan after breast repositioning is calibrated with the scan prerepositioning, but taken on the same day; and 3) SZ calibrated with S1, which indicates the level of change seen between successive monthly scans. Note that as each SZ is calibrated with S1, there is one less data point than there are patient scans for each patient.

The data presented in Fig. 6 help illustrate how well the system could serve the purpose of breast health monitoring application. For example, for V7-V9, the results indicate that

the maximum pixel intensity of scans over time (S2–SZ) are consistent within each volunteer, especially compared to the variability observed across all volunteers. Further, for patients with similar maximum pixel value ranges, variations in healthy breast scans do not readily alter the imaging results (as in Fig. 5 for V9). These results imply that monitoring techniques that differentiate between healthy and tumorous breasts may be implemented through computer-aided detection, or classification, of maximum pixel intensities.

For select other patient volunteers, we do observe a discrepancy in the maximum pixel intensities. Specifically, the maximum of V4 and V5 is three to five times greater than that of any other volunteer. This may be due to several factors, in addition to the relative positioning of the breast to the immersion medium. We postulate that the increased consistency in later volunteer scans (V7 and thereafter) originates from improved measurement routine and equipment usage. Further study also remains to be done to determine what pixel intensity variation constitutes appropriate levels of healthy tissue changes (the results shown here may well be within this range) and what levels indicate possible tumor presence.

D. Structural Similarity Index

Finally, we apply an image similarity metric, the structural similarity index (SSIM) [22], to compare images generated from successive scans of the same volunteer. This metric functions by studying the relationships between spatially-near pixels, as opposed to mean-square error or cross correlation similarity functions that compare image intensities on a pixel-to-pixel basis. All image comparisons are conducted based on only two images at a time (or in our case, two 2-D slices of the 3-D image). The SSIM uses three specific image qualities in order to produce a similarity value: the luminance, the contrast, and the structure. We first remove the mean intensity from each image to obtain zero-mean data. Then the standard deviation of values of each image is used to estimate the contrast; each image is then normalized for unit standard deviation. Finally, the normalized images are compared for structural content. The SSIM value is equal to one if the image under test is exactly identical to the reference image, and is equal to zero if the images share no similarities.

We present the SSIM values for the clinical data in Fig. 7. To obtain these results, differential images are used. In particular, we generate an image using the second scan of each volunteer (S2) calibrated with the first scan of each volunteer (S1). This image is denoted as "S2 cal S1" and it is the reference image for the SSIM calculation for each volunteer. The later scans of each volunteer (SZ, $Z > 2$) are calibrated with S1 ("SZ cal S1"). These remaining images are used as the comparison data for the SSIM. A single SSIM value is acquired for each set of two 3-D images that are under comparison. In particular, we calculated the SSIM for each 2-D slice, and then averaged over all slices in order to obtain a single output per 3-D image.

In Fig. 7, the SSIM values are plotted for each image of each volunteer. We note that there are no SSIM values for V6 as only
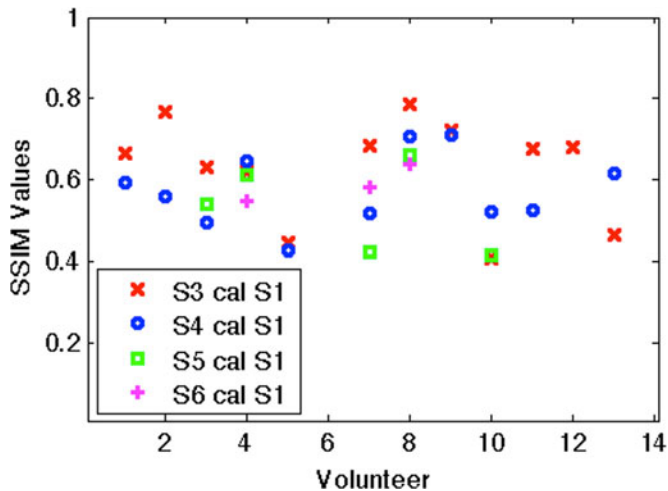
Fig. 7. Mean SSIM values for each image of each volunteer VY: the reference image is the image S2 calibrated with S1, while the images being compared are SZ ($Z > 2$) calibrated with S1 ("SZ cal S1"). There are a different number of points for each volunteer, as determined by the number of visits in which they had breast scans.

TABLE V
SUMMARY OF METRICS: THE MAXIMUM, MINIMUM, MEAN, MEDIAN AND STANDARD DEVIATION OVER ALL PATIENT SCANS, OF THE CROSS CORRELATION (XCORR), MAXIMUM PIXEL INTENSITY (MPI, dB) FOR S$_z$ SCANS, AND SSIM

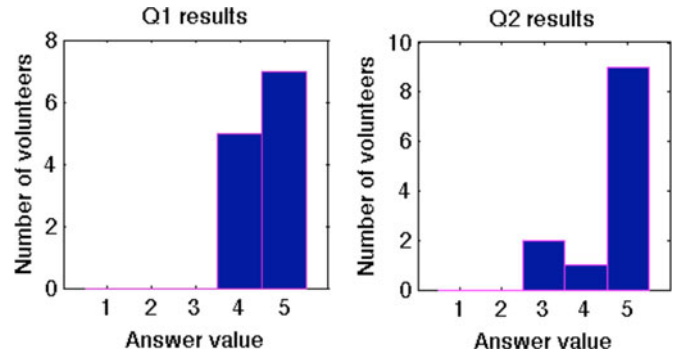|	XCORR	MPI (dB)	SSIM
Maximum	0.9947	45.7	0.7867
Mean	0.9372	8.59	0.5905
Median	0.9511	4.62	0.6111
Minimum	0.7593	0.13	0.4099
Standard Deviation	0.011	10.3	0.1066

Fig. 8. Histogram of results from patient feedback question: Question #1 (Q1, left plot): "On a scale of 1 to 5 (5 being the best), how comfortable was your scan?" and Question #2 (Q2, right plot) "On a scale of 1 to 5 (5 being the best), how would you rate the speed of the scan?"

two scans were recorded for this volunteer, S1 and S2, and thus there are no remaining scans for comparison purposes.

The SSIM values provide a measure of the change in the volunteer scans over time. From Fig. 7, it is clear that the similarity varies from scan to scan and patient to patient. As seen in the plot, the highest SSIM value is 0.79 for V8. The lowest value is 0.41, for V10. It is also seen that for some volunteers, for instance, V4 and V11, the SSIM values obtained from different images are closely grouped. Use of the SSIM metric may provide information about how much the breast changes over time, which is an important part of a breast health monitoring application.

V. DISCUSSION

In this section, we briefly compare the signal and imaging data. We then provide a summary of patient feedback, and finally discuss the potential improvements to our system, based on the results shown in this study.

A. Comparison of Results

A summary of applying the three-presented metrics to the collected data is provided in Table V. The data are taken from within scans of a given patient, over all patients. In other words, the results summarize what values can be expected for a new scan, based on a previous scan of that same patient. This is in contrast to the "interpatient" data, which are shown on the right of Fig. 4, that demonstrates the range of values expected if you were to compare breast scans from one patient to scans from another, different patient. In Table V, the cross correlation and SSIM are as defined in relation to Figs. 4 and 7, respectively. The maximum pixel intensity is presented in decibels, and here indicates the difference in maximum pixel intensities between scans of the same patient.

Thorough studies must be performed to identify what types of changes in signals and images could indicate tumor growth versus healthy, regular breast changes. In particular, a similar clinical study must be performed on patients with breast cancer to confirm that the imaging system can successfully detect a tumor. It is also relevant to note that healthy changes in breast tissue may still signify an increase in risk for developing cancer; it was demonstrated that breast tissues that increase in density over modest time periods (three years) have an increased breast cancer risk whereas women with a decrease in tissue density were at decreased risk [23].

B. Patient Feedback

We asked patients to fill out an exit questionnaire after participating in their first breast scan. Of the 13 women, 12 completed the questionnaire. Patients were asked about the level of comfort and speed of the scan, on a scale from 1 to 5 (5 being the best); results are presented in Fig. 8. A final binary question asking *"Were you comfortable resting in the scan position (yes/no)?"* resulted in 83% *"yes."* All patient volunteers were happy to return for future scans. This encouraging outcome confirms that our microwave imaging system is progressing in the right direction, in terms of fast and comfortable scans.

C. Directions for Future Improvements

From the clinical data and analysis, we have been able to identify multiple areas in which the system components and measurement parameters can be improved.

First, we summarize physical system modifications that could lead to more consistent data collection. The results presented here, together with our work in [19], suggest that patient positioning within the radome can affect the collected data if it is not well controlled. With our current system design, it is a challenge to accurately reposition the patient. The system would be more robust if: 1) a smaller radome is used, allowing less room for breast movement; and 2) the need for an immersion medium can be eliminated, or at least a semisolid material can be used in place of the gel-like ultrasound (so that there is no uncertainty in the immersion volume or distribution around the breast).

Second, we can improve the data collection process. In particular, using a higher sampling rate can result in more accurate relative permittivity estimates. By using samples that are spaced more closely in time we can reduce the uncertainty in the location of major peaks of the signal; this will improve time-alignment of the data and time-delay calculations.

VI. Conclusion

In this study, we have presented results of a time-domain microwave radar system applied to clinical trials of breast health monitoring. We have scanned 13 healthy patient volunteers a total of 342 times, with each patient having scans done over a period ranging from two to eight months. The data for successive scans of each patient have been analyzed in terms of similarity of the collected signals, and in terms of the reconstructed breast images. An important outcome of the study is the identification of the variability that should be expected when calculating metrics from scans recorded on different days from the same healthy patient. By specifying this variability, we have provided a baseline for future studies that involve scans of breasts that are known to contain tumors.

The results show promise for monitoring, with repeatable breast scans for several patients. The lack of consistency for other patients has motivated us to identify multiple factors that can be addressed to improve the system performance, allowing us to progress toward the construction a successful breast health-monitoring device. Near-future work will include testing our system's response and sensitivity to breast scanning of volunteers with malignant growths.

References

[1] American Cancer Society, "Facts and figures 2014," 2014.

[2] M. T. Mandelson *et al.*, "Breast density as a predictor of mammographic detection: Comparison of interval- and screen- detected cancers," *J. Nat. Cancer Inst.*, vol. 92, no. 13, pp. 1081–1087, Jul. 2000.

[3] M. Lazebnik *et al.*, "A large-scale study of the ultrawideband microwave dielectric properties of normal, benign and malignant breast tissues ob-

tained from cancer surgeries," *Phys. Med. Biol.*, vol. 52, no. 20, pp. 6093–6115, 2007.

[4] T. Grzegorczyk *et al.*, "Fast 3-D tomographic microwave imaging for breast cancer detection," *IEEE Trans. Med. Imag.*, vol. 31, no. 8, pp. 1584–1592, Aug. 2012.

[5] J. Bourqui *et al.*, "A prototype system for measuring microwave frequency reflections from the breast," *Int. J. Biomed. Imag.*, vol. 2012, pp. 1–12, 2012.

[6] H. Jiang *et al.*, "Ultrasound-guided microwave imaging of breast cancer: Tissue phantom and pilot clinical experiments," *Med. Phys.*, vol. 32, no. 8, pp. 2528–2535, Aug. 2005.

[7] M. Klemm *et al.*, "Clinical trials of a UWB imaging radar for breast cancer," in *Proc. Eur. Conf. Antennas Propag.*, Apr. 2010, pp. 1–4.

[8] E. C. Fear *et al.*, "Microwave breast imaging with a monostatic radar-based system: A study of application to patients," *IEEE Trans. Microw. Theory Techn.*, vol. 61, no. 5, pp. 2119–2128, May 2013.

[9] T. M. Grzegorczyk *et al.*, "Microwave tomographic imaging for breast cancer chemotherapy monitoring," in *Proc. Eur. Conf. Antennas Propag.*, Apr. 2014, pp. 702–703.

[10] X. Zeng *et al.*, "Experimental investigation of the accuracy of an ultrawideband time-domain microwave-tomographic system," *IEEE Trans. Instrum. Meas.*, vol. 60, no. 12, pp. 3939–3949, Dec. 2011.

[11] E. Porter *et al.*, "Time-domain multistatic radar system for microwave breast screening," *IEEE Antennas Wireless Propag. Lett.*, vol. 12, no. 1, pp. 229–232, Feb. 2013.

[12] E. Porter *et al.*, "Breast monitoring via time-domain microwave radar: Early clinical trial study," in *Proc. Ann. Int. Conf. IEEE Eng. Med. Biol. Soc.*, Aug. 2014, pp. 6601–6604.

[13] E. Porter *et al.*, "Breast tissue screening with microwave time-domain radar: Initial clinical trials," in *Proc. IEEE Int. Conf. Antenna Meas. Appl.*, Nov. 2014, pp. 1–4.

[14] E. Porter *et al.*, "Microwave time-domain radar: Healthy tissue variations over the menstrual cycle," *IEEE Antennas Wireless Propag. Lett.*, vol. 14, no. 1, pp. 1310–1313, Feb. 2015.

[15] A. Santorelli *et al.*, "Image classification for a time-domain microwave radar system: Experiments with stable modular breast phantoms," in *Proc. Eur. Conf. Antennas Propag.*, Apr. 2015, pp. 1–5.

[16] A. Santorelli *et al.*, "Experimental demonstration of pulse shaping for time-domain microwave breast imaging," *Prog. Electromagn. Res.*, vol. 133, pp. 309–329, 2013.

[17] H. Kanj and M. Popović, "A novel ultra-compact broadband antenna for microwave breast tumor detection," *Prog. Electromagn. Res.*, vol. 86, pp. 169–198, 2008.

[18] E. Porter *et al.*, "Time-domain microwave radar applied to breast imaging: Measurement reliability in a clinical setting," *Prog. Electromagn. Res.*, vol. 149, pp. 119–132, 2014.

[19] P. C. Stomper *et al.*, "Analysis of parenchymal density on mammograms in 1353 women 25–79 years old," *Am. J. Roentgenol.*, vol. 167, no. 5, pp. 1261–1265, Nov. 1996.

[20] E. Porter *et al.*, "Measurement uncertainties in differential radar applied to breast imaging," in *Proc. IEEE Sensors Appl. Symp.*, 2014, pp. 6–10.

[21] H. B. Lim *et al.*, "Confocal microwave imaging for breast cancer detection: Delay-multiply-and-sum image reconstruction algorithm," *IEEE Trans. Biomed. Eng.*, vol. 55, no. 6, pp. 1697–1704, Jun. 2008.

[22] Z. Wang *et al.*, "Image quality assessment: From error visibility to structural similarity," *IEEE Trans. Image Process.*, vol. 13, no. 4, pp. 600–612, Apr. 2004.

[23] K. Kerlikowske *et al.*, "Longitudinal measurement of clinical mammographic breast density to improve estimation of breast cancer risk," *J. Nat. Cancer Inst.*, vol. 99, no. 5, pp. 386–395, Mar. 2007.

Authors' photographs and biographies not available at the time of publication.